Article | Open Access

Energy Z

Liu *et al. Energy Z* **2026**, *2*, 200025 **DOI:**10.20517/energyz.2026.32

Intergranular and microstructural evolution regulates mechanical and ion-transport properties of NaSICON-type solid electrolytes

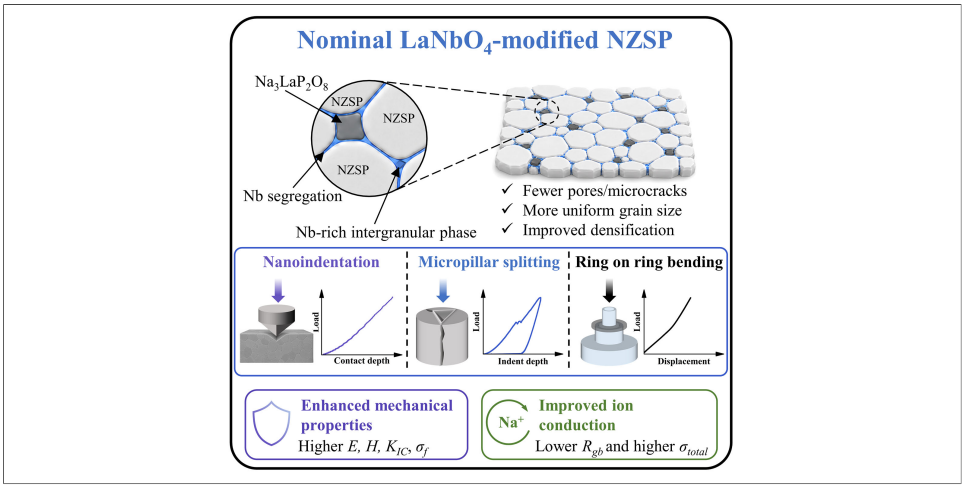
Xingyu Liu[1,*], Qianli Ma[2], Frank Tietz[2,3], Jürgen Malzbender[1], Ruth Schwaiger[1,4]

Keywords:
NaSICON solid electrolyte, mechanical properties, ionic conductivity, grain-boundary engineering

Citation: Liu, X.; Ma, Q.; Tietz, F.; Malzbender, J.; Schwaiger, R. Intergranular and microstructural evolution regulates mechanical and ion-transport properties of NaSICON-type solid electrolytes. *Energy Z* **2026**, *2*, 200025. https://dx.doi.org/10.20517/energyz.2026.32

Received: 18 Aug 2026
First Decision: 30 Sep 2026
Revised: 20 Oct 2026
Accepted: 4 Nov 2026
Published: 27 Nov 2026

Academic Editor:
Yuping Wu
Copy Editor:
Shu-Yuan Duan
Production Editor:
Shu-Yuan Duan



Abstract

Ionic transport and mechanical integrity are critical to the performance of ceramic solid electrolytes in solid-state batteries. Although grain-boundary engineering improves ionic transport, its effects on mechanical properties remain unclear. Here, the impact of nominal $LaNbO_4$ (LN) additions on the mechanical properties and ionic transport behavior of the solid electrolyte $Na_{3.4}Zr_2Si_{2.4}P_{0.6}O_{12}$ (NZSP) is investigated. The results show that LN reacts with NZSP during processing, forming $Na_3LaP_2O_8$ and Nb-rich intergranular regions. The $Na_3LaP_2O_8$ phase affects the microstructure by reducing grain-size heterogeneity and limiting microcrack formation, while the Nb-rich intergranular regions, distributed along grain boundaries and residual pores, may contribute to improved densification. Among the samples examined, the NZSP sample with 2 mol% LN exhibits enhanced mechanical properties together with a 79% increase in ionic conductivity; compared with the unmodified sample, the elastic modulus, hardness, and fracture toughness increase by

[1]Forschungszentrum Jülich GmbH, Institute of Energy Materials and Devices, Structure and Function of Materials (IMD-1), Jülich 52425, Germany.
[2]Forschungszentrum Jülich GmbH, Institute of Energy Materials and Devices, Materials Synthesis and Processing (IMD-2), Jülich 52425, Germany.
[3]Forschungszentrum Jülich GmbH, Institute of Energy Materials and Devices, Helmholtz Institute Münster - Ionics in Energy Storage (IMD-4), Jülich 52425, Germany.
[4]Chair of Energy Engineering Materials, Faculty 5, RWTH Aachen University, Aachen 52056, Germany.

[*]**Correspondence to:** Xingyu Liu, Forschungszentrum Jülich GmbH, Institute of Energy Materials and Devices, Structure and Function of Materials (IMD-1), 52425 Jülich, Germany. E-mail: xing.liu@fz-juelich.de

approximately 14%, 40%, and 82%, respectively, while the mean fracture strength is approximately 11% higher. With further increases in LN content, the ionic conductivity decreases, while the fracture toughness of 10LN falls below that of 2LN and 5LN but remains higher than that of pristine NZSP. These findings highlight the influence of LN-induced microstructural evolution on mechanical properties and ionic transport in the investigated NZSP samples, providing insights into the development of NaSICON-type solid electrolytes for solid-state sodium batteries.

INTRODUCTION

The demand for high-energy-density energy storage systems has intensified safety concerns related to flammable liquid electrolytes in conventional lithium and sodium batteries, including leakage and thermal runaway[1,2]. All-solid-state batteries (ASSBs) based on inorganic solid electrolytes offer improved safety and the potential for high energy density[3,4]. Among emerging systems, sodium-based ASSBs are particularly promising for large-scale energy storage due to the abundant supply, affordability, and broad geographical availability of sodium[5]. This has driven extensive efforts toward the development of high-performance Na^+ solid electrolytes.

Sodium superionic conductor (NaSICON) materials are promising sodium-ion solid electrolytes owing to their three-dimensional Na^+ migration pathways, high ionic conductivity at room temperature (RT), and structural stability[6,7]. Among them, $Na_{1+x}Zr_2Si_xP_{3-x}O_{12}$ ($2 \le x \le 2.6$, especially $x = 2.4$; NZSP) is a leading candidate. It delivers an ionic conductivity of 10^{-3}-10^{-2} $S \cdot cm^{-1}$ at RT, together with good chemical stability and compatibility with sodium metal[6,8]. Even though the conductivity is nearly the same as that of liquid electrolytes[9], improving the microstructure can lead to a further reduction in grain-boundary resistance. At grain boundaries, incomplete densification and anisotropic grain expansion[8] can generate pores and microcracks[10], while detrimental grain-boundary segregation can increase grain-boundary resistance[11]. These features hamper Na^+ migration. Consequently, grain-boundary engineering via aliovalent substitutions, non-stoichiometries or formation of secondary phases has been extensively investigated. Representative strategies include Mg-induced formation of $NaMgPO_4$ as an intergranular phase that reduces grain-boundary resistance[12], and Na_2SiO_3 addition promoting pore filling and Si-rich grain-boundary phases[13]. These approaches demonstrate that tailoring grain-boundary chemistry and structure is an effective route to improve the overall ionic conductivity of NZSP.

Nevertheless, improved transport properties alone may not be sufficient to guarantee long-term performance stability. Solid electrolytes in practical devices must withstand stack pressure and stress fluctuations associated with sodium plating and stripping. Inadequate mechanical robustness can induce microcracks and local mechanical instability. This promotes current constriction and preferential sodium deposition at defect sites, increasing the risk of short-circuiting[14,15]. Intrinsic mechanical properties, including elastic modulus, hardness, fracture toughness, and fracture strength, are therefore critical for evaluating resistance to deformation and crack propagation. These properties are closely linked to the structural integrity and service reliability of solid electrolytes[16,17]. Although previous studies have examined the influence of sintering conditions and elemental substitutions on the mechanical properties of NZSP[18,19], the mechanical consequences of grain-boundary engineering using secondary phases-either added or in-situ formed phases that promote densification and ionic transport at grain boundaries-remain largely unexplored.

Our previous study showed that 2 mol% nominal $LaNbO_4$ (LN) modification has a beneficial effect on grain-boundary ion transport in $Na_{3.4}Zr_2Si_{2.4}P_{0.6}O_{12}$[8]. Building on this work, the present study extends the investigation to a broader LN-content range, with emphasis on composition-dependent mechanical behavior and its correlation with microstructural evolution and ionic transport. Elastic modulus, hardness, fracture

toughness, and fracture strength are systematically evaluated and correlated with the corresponding microstructural and transport behavior. The results reveal a chemical reaction of LN with NZSP, leading to the formation of $Na_3LaP_2O_8$ and Nb-rich intergranular regions. Mechanical properties and ionic transport evolve differently with increasing LN content, indicating their distinct sensitivities to intergranular and microstructural evolution.

EXPERIMENTAL

Sample preparation

The powders were synthesized through a solution-assisted solid-state reaction route. Stoichiometric amounts of $NaNO_3$ [VWR International, 99%, Chemically Pure (CP)] and $ZrO(NO_3)_2$ (Sigma-Aldrich, 99%, CP) were first dissolved in deionized water to obtain a transparent precursor solution. $Si(OCH_2CH_3)_4$ [Merck KGaA, 99%, Analytical Reagent (AR)] was added to the solution in the required stoichiometric amount under stirring at RT (360 rpm), and the mixture was stirred for 1 h. After complete hydrolysis, $NH_4H_2PO_4$ (Merck KGaA, 99%, AR) was added gradually while maintaining continuous agitation, leading to rapid conversion of the homogeneous solution into a suspension containing zirconium oxyphosphate. For LN-containing NZSP, stoichiometric amounts of $NH_4NbO(C_2O_4)_2$ (Aldrich, 99%, AR) and $La(NO_3)_3{\cdot}6H_2O$ (Aldrich, 99%, AR) were additionally incorporated into the precursor solution at the early mixing stage to obtain the targeted composition.

The resulting slurry was dried at 85 °C, followed by calcination at 800 °C for 3 h to yield a white powder. Following calcination, the product was dispersed in ethanol and milled with zirconia balls for 48 h. The resulting material was subsequently dried at 70 °C for 12 h. Pellets for impedance measurements were prepared from both pristine and modified powders by uniaxial compaction in a 13 mm cylindrical die at RT under ~ 113 MPa, followed by sintering at 1,260 °C for 5 h. The sintered pellets were approximately 10 mm in diameter and 1-2 mm in thickness. Table 1 summarizes the compositions of the materials investigated in this work. The impedance data for pristine NZSP and 2LN were taken from Ref.[8], whereas 1LN, 5LN, and 10LN were each measured using one pellet in the present work.

Characterization

Specimens for mechanical testing were prepared using a 16 mm die and had sintered dimensions of approximately 12.5 mm in diameter and 0.8 mm in thickness. The cross-sections of the specimens were metallographically prepared for mechanical testing and microstructural characterization. Sequential grinding was carried out with 80-2,500 grit SiC papers, followed by polishing with 3-0.5 μm diamond suspensions and an anhydrous lubricant.

Phase identification was performed by X-ray diffraction (XRD) using an EMPYREAN diffractometer (PANalytical, Kassel, Germany) and Cu Kα radiation. Quantitative phase fractions and lattice constants were further obtained by Rietveld refinement using TOPAS v.6 (Bruker AXS). Structural models required for the refinement were retrieved from the Inorganic Crystal Structure Database (ICSD). Prior to XRD analysis, all sintered specimens were pulverized to fine powders to improve measurement reliability. The microstructure of the iridium-coated surfaces was examined using a field-emission scanning electron microscope (FE-SEM, MERLIN™, Carl Zeiss Microscopy, Oberkochen, Germany). Elemental distribution and phase chemistry were obtained using energy-dispersive X-ray spectroscopy (EDX, X-Max 80, Oxford Instruments, UK). Micro-pillars were prepared using a plasma-focused ion beam scanning electron microscope (PFIB-SEM, Helios 5, Thermo Fisher Scientific, US). The pillars were fabricated by ion-beam milling to a height of approximately 5 μm, with the diameter maintained approximately equal to the pillar height. SEM images were analyzed using ImageJ to determine the porosity[20].

Table 1. Nominal compositions of the investigated materials

Material	Label
$Na_{3.4}Zr_2Si_{2.4}P_{0.6}O_{12}$	Pristine
$Na_{3.4}Zr_2Si_{2.4}P_{0.6}O_{12}$ + 1 mol% LN	1LN
$Na_{3.4}Zr_2Si_{2.4}P_{0.6}O_{12}$ + 2 mol% LN	2LN
$Na_{3.4}Zr_2Si_{2.4}P_{0.6}O_{12}$ + 5 mol% LN	5LN
$Na_{3.4}Zr_2Si_{2.4}P_{0.6}O_{12}$ + 10 mol% LN	10LN

LN: $LaNbO_4$.

To expose the grain boundaries for grain-size evaluation, the polished pellets were thermally etched (i.e., heat-treated to reveal the grain boundaries) at 1,100 °C for 1 h, followed by furnace cooling to RT. For the LN-modified samples, grain-size distributions were determined by ImageJ analysis of three SEM images acquired from different regions of each sample. Approximately 300-500 grains were analyzed in each image. The reported grain sizes correspond to measurements from two-dimensional SEM images.

Symmetric Au | NZSP (-LN) | Au cells were prepared by sputtering Au electrodes onto both pellet faces (Cressington 108 Auto, Cressington Scientific Instruments Ltd., UK; supplied by Ted Pella Inc., USA). Impedance measurements at RT were performed using an Alpha-A analyzer (Alpha-A, Novocontrol Technologies GmbH & Co. KG, Germany) over the frequency range of 3 MHz to 1 Hz with an alternating current (AC) voltage amplitude of 20 mV. The spectra were fitted using Z-View (Scribner Associates Inc., USA). To enable direct comparison among samples with slightly different dimensions, the impedance data were normalized to the sample geometry. The fitted resistance values were converted to geometry-normalized resistance values according to[21]:

$$R_{\text{norm}} = RA/L \tag{1}$$

where R is the raw resistance obtained from impedance fitting, A is the electrode area, and L is the pellet thickness. Accordingly, the ionic conductivity was then calculated as the reciprocal of the geometry-normalized resistance, $\sigma = 1/R_{norm}$.

Mechanical testing

Nanoindentation measurements were performed at RT on polished cross-sections using a G200X instrument (KLA Instruments, Milpitas, CA, USA). A diamond Berkovich indenter was used for all measurements. A 6 × 6 indentation array was applied to evaluate the elastic modulus (E) and hardness (H). Testing was conducted in continuous stiffness measurement (CSM) mode at a strain rate of 0.2 s^{-1}, an excitation frequency of 110 Hz, and a displacement oscillation of 2 nm, allowing both properties to be monitored throughout the indentation depth.

Pillar-splitting experiments were conducted using a Berkovich tip mounted on an FT-NMT04 *in situ* nanoindenter (FemtoTools AG; part of Oxford Instruments, UK). The splitting threshold was identified from the measured load-displacement response, and the fracture toughness was then calculated according to[22]:

$$K_{IC} = \gamma \times \frac{P_c}{R^{3/2}} \tag{2}$$

where R is the pillar radius, P_c is the critical load at which splitting occurs, and γ is a dimensionless factor related to the indenter geometry and the elastic-plastic response and crack evolution of the material. The γ

value was evaluated using[22,23]:

$$\gamma = 0.0149\left(\frac{E}{H}\right) + 0.057 \tag{3}$$

For each composition, E and H were calculated from no fewer than 36 indents distributed across the polished surface of a representative pellet. K_{IC} was evaluated from at least 6 pillar-splitting tests on the same pellet.

Fracture strength was evaluated by a ring-on-ring (ROR) bending test at room temperature. Each pellet was placed on a supporting ring (diameter 10.032 mm) and loaded by a smaller loading ring (diameter 3.324 mm) until failure, from which the fracture strength was determined. In the present study, ROR tests were conducted on 5 specimens for each LN-modified sample except 2LN. An INSTRON 1362 electromechanical test frame fitted with a ± 1,000 N Lebow load cell was used for the measurements. Specimen deflection was tracked by a Solartron Metrology linear variable differential transformer coupled to a ceramic push rod. The peak tensile stress was calculated in accordance with ASTM C1499-05 using[24]:

$$\sigma_f = \frac{3(1+v)\times F_f}{2\pi\times t^2}\left[\ln\frac{r_2}{r_1} + \left(\frac{1-v}{1+v}\right)\times\left(\frac{r_2^2 - r_1^2}{2r_3^2}\right)\right] \tag{4}$$

where v is the Poisson's ratio (0.27), t denotes the specimen thickness, and F_f is the fracture load. The parameters r_1, r_2, and r_3 correspond to the radii of the loading ring, supporting ring, and specimen, respectively. According to the standard, Weibull statistical analysis is not recommended for the limited number of specimens used in the present work (< 30 per composition). Therefore, the fracture strength is reported as the mean value with the corresponding standard deviation, following the recommendation of the standard.

For clarity, selected previously published data are included as reference data in this study. The XRD data, Rietveld-derived phase fractions, grain-size distribution, micropillar radius, and critical splitting load of pristine NZSP were taken from Ref.[25]. The fracture-strength data for pristine NZSP (18 specimens) and 2LN (6 specimens), together with the impedance data for these two compositions, were taken from Ref.[8]. All other data were newly acquired in the present study.

RESULTS AND DISCUSSION

Phase composition and microstructural evolution

The XRD patterns of all samples are presented in Figure 1, and the phase fractions obtained from Rietveld refinement, normalized to the identified crystalline phases, are summarized in Table 2. As shown in Figure 1A, all retain NZSP as the primary crystalline phase after LN addition. Figure 1B presents a magnified view of the diffraction profiles between 20° and 40° in 2θ, where reflections from secondary phases can be identified. ZrO_2 is detected in both pristine and LN-modified samples. No diffraction peaks associated with residual LN are observed even at an addition level of 10 mol%. Instead, $Na_3LaP_2O_8$ emerges as a new secondary phase, and its diffraction peak intensities gradually increase with increasing LN content. In addition, refinement reveals non-monotonic variations in the lattice parameters of the NZSP phase with LN addition, and the corresponding values are summarized in Supplementary Table 1.

Figure 2A-E shows representative backscattered SEM images of pristine and LN-modified NZSP samples, revealing distinct phase contrasts and changes in microstructural defects. The pristine NZSP contains abundant microcracks distributed mainly along grain boundaries [Figure 2A]. After LN modification, the

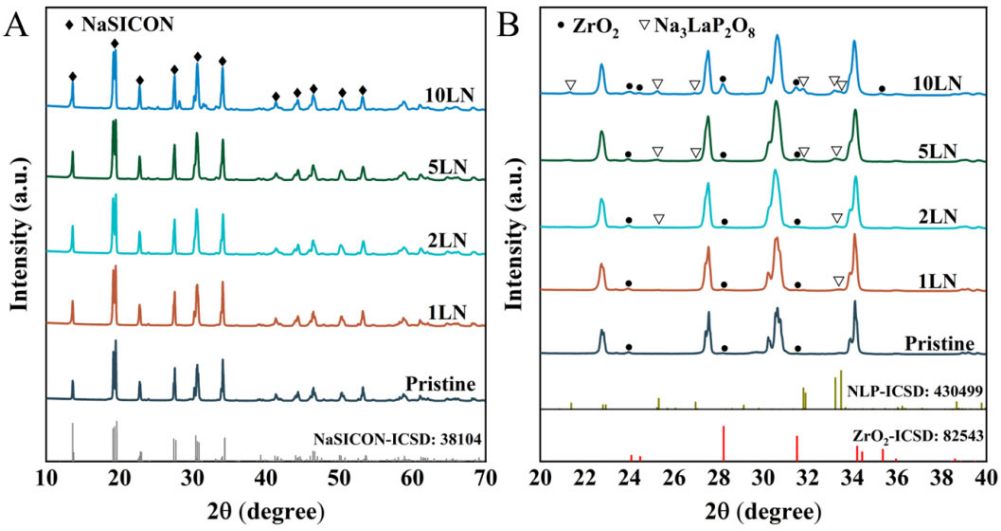


Figure 1. XRD patterns of (A) all samples and (B) the enlarged 2θ range of 20-40°. The pristine NZSP XRD data were taken from Ref.[25] and replotted here. All samples exhibit a well-crystallized NZSP main phase. ZrO_2 is detected in both pristine and LN-modified samples, whereas $Na_3LaP_2O_8$ appears only in the LN-modified samples. LN: $LaNbO_4$; ICSD: Inorganic Crystal Structure Database; XRD: X-ray diffraction; NZSP: $Na_{3.4}Zr_2Si_{2.4}P_{0.6}O_{12}$.

Table 2. Phase fractions (wt%) of the NZSP main phase and secondary phases obtained from Rietveld refinement

	Pristine[25]	1LN	2LN	5LN	10LN
NZSP	99.7	98.8	98.2	95.7	87.5
$Na_3LaP_2O_8$	0	0.7	1.3	3.7	6.0
ZrO_2	0.3	0.6	0.6	0.6	6.5

NZSP: $Na_{3.4}Zr_2Si_{2.4}P_{0.6}O_{12}$; LN: $LaNbO_4$.

density of microcracks is significantly reduced. In particular, microcracks are nearly absent in 2LN [Figure 2C] and 5LN [Figure 2D], while they become discernible again at higher LN content (10LN). EDX was employed to determine the composition of the secondary phases in the LN-modified NZSP samples. Figure 2F-H presents the EDX results for the 2LN sample, and the results for the other LN-modified NZSP samples are similar. The elemental mapping in Figure 2F and H reveals that Nb is enriched in the dark regions, whereas La is significantly concentrated in the light regions. Further support for this interpretation is provided by the line-scan profile in Figure 2G. In combination with the XRD results, the La-rich regions can be identified as $Na_3LaP_2O_8$, while the Nb-rich features are assigned to intergranular regions.

Rietveld refinement shows non-monotonic variations in the NZSP lattice parameters, while the $Na_3LaP_2O_8$ fraction increases with increasing LN addition. A La mass-balance analysis in Supplementary Table 2 further shows that the refined $Na_3LaP_2O_8$ fractions are in reasonable agreement with those expected from the nominal La addition, suggesting that La is predominantly accommodated in $Na_3LaP_2O_8$ rather than substantially incorporated into the NZSP lattice. These results suggest that LN interacts with NZSP during sintering, promoting the formation of $Na_3LaP_2O_8$ and Nb-rich intergranular regions. The ZrO_2 content increases for 10LN compared with the lower-LN compositions, which may be related to increased Zr redistribution at higher LN contents.

Representative porosity and grain-morphology images of pristine NZSP, 2LN, and 10LN are shown in Figure 3A-F, while the corresponding quantitative analyses for all compositions are summarized in Figure 3G and H. The porosity was quantified by determining the void fraction from cross-sectional images collected at

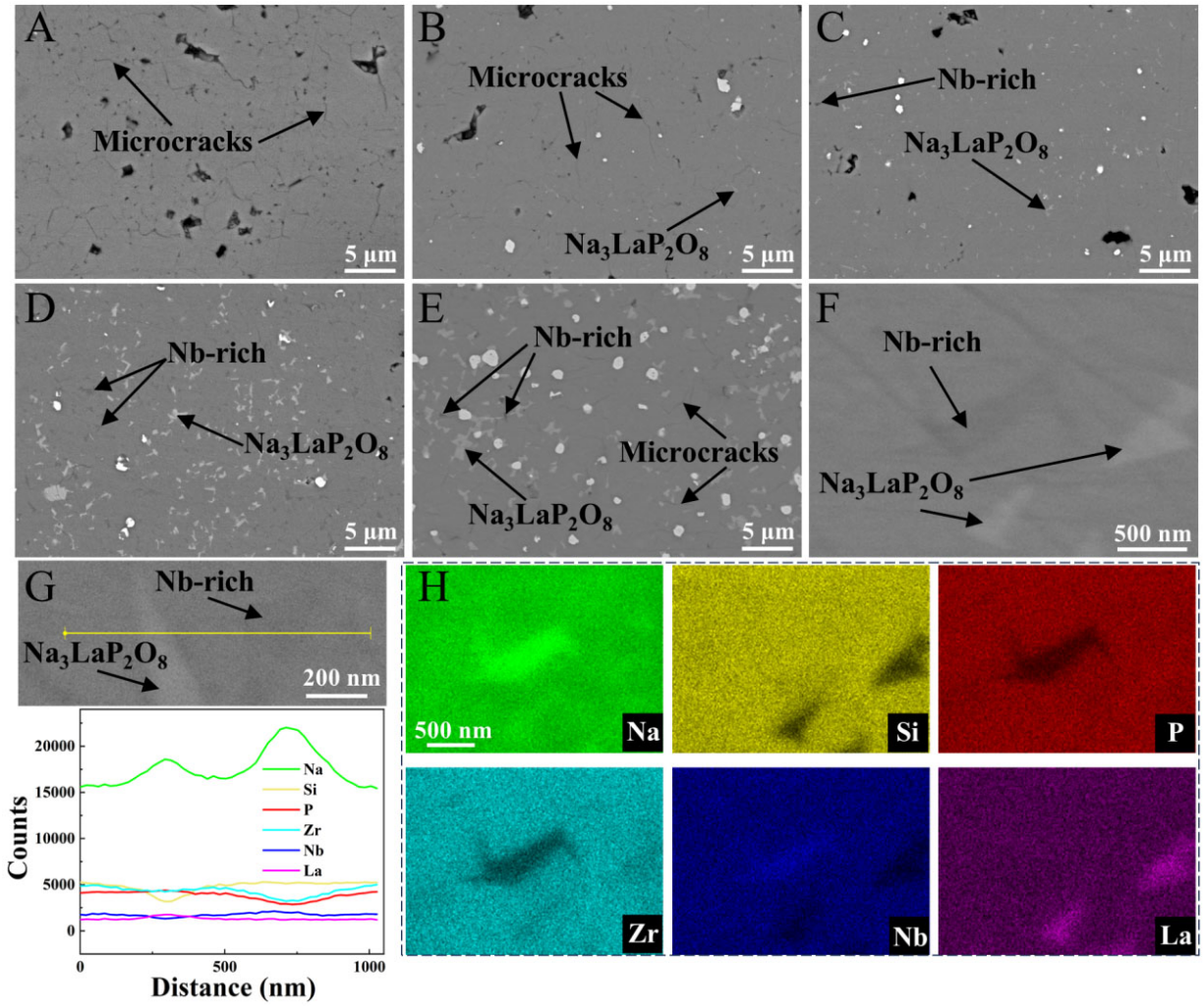


Figure 2. Backscattered SEM images and EDX analysis of pristine and LN-modified NZSP samples. (A-E) Backscattered SEM images of pristine NZSP, 1LN, 2LN, 5LN, and 10LN, respectively. The bright spherical grains correspond to ZrO_2; $Na_3LaP_2O_8$ appears brighter than the NZSP matrix, and Nb-rich intergranular regions show the darkest contrast; (F-H) EDX analysis of the 2LN sample. (F) EDX elemental mapping region showing regions with different backscattered-electron contrasts; (G) Selected region for line scanning and the corresponding EDX line-scan profiles, where the $Na_3LaP_2O_8$ phase shows reduced Nb, Zr, and Si contents, and the Nb-rich intergranular region exhibits decreased P and Zr contents with nearly unchanged Si; (H) Corresponding EDX elemental maps of the region shown in (F), with the scale bar in the Na map applying to all maps. SEM: Scanning electron microscope; EDX: energy-dispersive X-ray spectroscopy; NZSP: $Na_{3.4}Zr_2Si_{2.4}P_{0.6}O_{12}$; LN: $LaNbO_4$.

different regions. Compared with pristine NZSP, all LN-modified samples show a markedly reduced porosity, indicating improved densification. Among them, 2LN and 5LN exhibit the lowest porosity, whereas 10LN shows a slight increase due to the presence of relatively large spherical pores.

For grain size analysis, the samples were subjected to thermal etching. Thermal etching reveals polygonal, equiaxed NZSP grains with clearly distinguishable grain boundaries [Figure 3D-F]. Pristine NZSP exhibits considerable variation in grain size. Most grains fall between approximately 1 and 5 μm, while a limited number of coarser grains reach about 7-8 μm. After LN incorporation, the distribution becomes noticeably more homogeneous and is dominated by grains measuring 1-3 μm.

The reduced porosity and more uniform grain-size distribution indicate improved densification and microstructural homogeneity upon LN modification. As observed earlier in the backscattered SEM images and EDX line-scan results [Figure 2], both $Na_3LaP_2O_8$ and the Nb-rich intergranular regions are in intimate

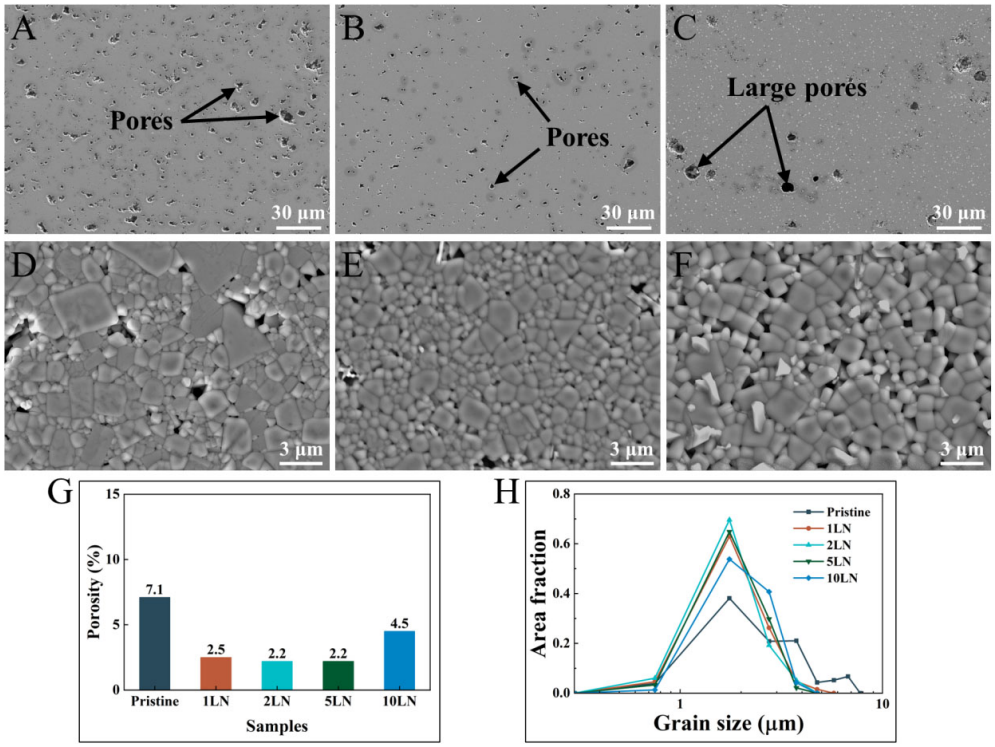


Figure 3. Porosity and grain-morphology characterization of pristine and LN-modified NZSP samples. (A-C) Representative porosity images of pristine NZSP, 2LN, and 10LN, respectively; (D-F) Representative grain morphologies of pristine NZSP, 2LN, and 10LN, respectively; (G) Porosity statistics for all samples; (H) Corresponding grain-size distributions for all samples, with the pristine NZSP data taken from Ref.[25]. The LN-modified samples show reduced porosity and grain size, together with a more uniform size distribution. LN: $LaNbO_4$; NZSP: $Na_{3.4}Zr_2Si_{2.4}P_{0.6}O_{12}$.

contact with the NZSP matrix and become more pronounced at grain boundaries and in intergranular regions with increasing LN modification. The formation of $Na_3LaP_2O_8$ along grain boundaries suppresses abnormal grain growth via a pinning effect, contributing to a more uniform grain structure [Figure 3]. Since oversized grains can exacerbate thermal-strain incompatibility during cooling and promote intergranular microcracking[26], the combined suppression of abnormal grain growth and reduction of residual porosity likely contribute to the mitigation of microcrack formation [Figure 2C]. However, for 10LN, the increased ZrO_2 content may promote microcracking[27] and contribute to the higher residual porosity.

Mechanical properties and strengthening mechanisms

Mechanical-properties evolution

Figure 4 compares the elastic modulus, hardness and fracture toughness of pristine NZSP and the LN-modified samples, together with representative micropillar morphologies. The corresponding mechanical properties are summarized in Table 3. For all samples, both *E* and *H* slightly decrease with increasing contact depth, which is commonly attributed to porosity and weak grain-boundary effects in polycrystalline ceramics[18]. The pristine NZSP presents the lowest *E* and *H*, whereas higher values are measured for all LN-modified samples. Among them, 2LN and 5LN follow similar trends and deliver the highest values of *E* (97.3 ± 3.6 and 98.1 ± 2.7 GPa, respectively) and *H* (7.7 ± 0.3 and 7.9 ± 0.3 GPa, respectively). In addition, 1LN has a higher *E* than 10LN, whereas their *H* values remain similar. This small difference in *H* may be related to the higher ZrO_2 fraction in 10LN, as evidenced by the indentation imprints in Supplementary Figure 1.

Values are reported as mean ± standard deviation. For *E*, *H*, and K_{IC}, the reported values are based on repeated measurements on one representative pellet per composition. To minimize the effects of surface roughness and indentation size at shallow depths, the average values obtained at contact depths above 200

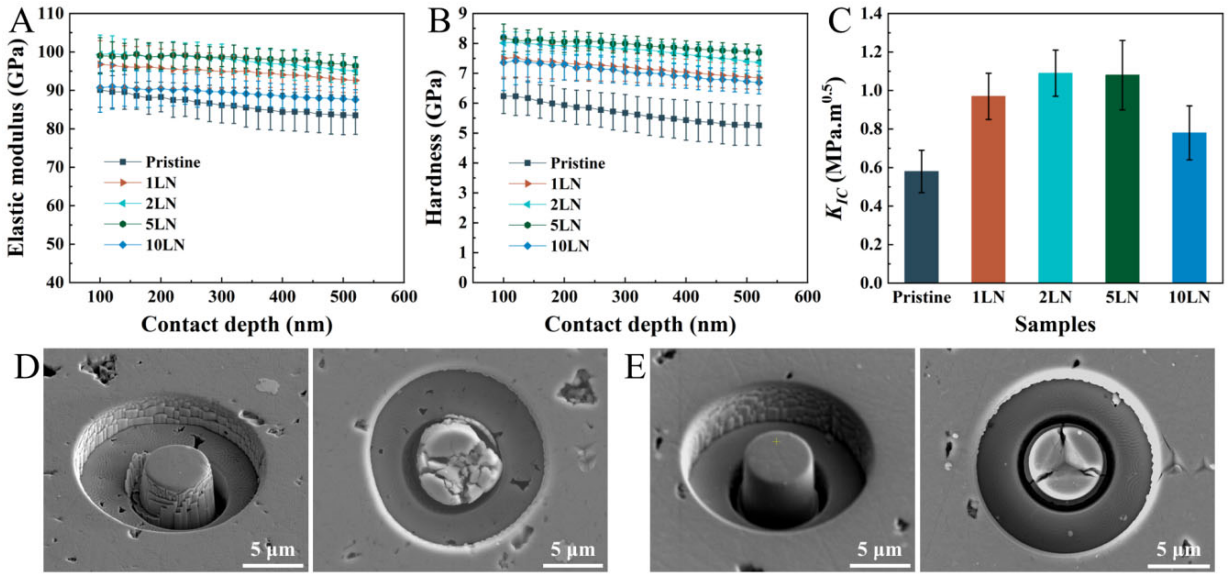


Figure 4. Mechanical characterization of pristine and LN-modified NZSP samples. (A and B) Elastic modulus and hardness as a function of indentation contact depth; (C) Fracture toughness values of all samples; (D and E) Representative SEM images of micropillars before and after splitting for pristine NZSP and 2LN, respectively. Error bars represent the standard deviation (SD) of measurements on one representative pellet per composition ($n \geq 36$ indentations for A and B; $n \geq 6$ micropillars for C). The 2LN and 5LN samples exhibit the highest elastic modulus, hardness and fracture toughness. LN: $LaNbO_4$; NZSP: $Na_{3.4}Zr_2Si_{2.4}P_{0.6}O_{12}$.

Table 3. Summary of mechanical properties of pristine and LN-modified NZSP samples

Sample	Elastic modulus, *E* (GPa)	Hardness, *H* (GPa)	Fracture toughness, K_{IC} (MPa•m$^{0.5}$)	Fracture strength, σ_f (MPa)
Pristine	85.4 ± 4.8	5.5 ± 0.6	0.60 ± 0.10	79 ± 13[8]
1LN	94.4 ± 4.0	7.1 ± 0.5	0.97 ± 0.12	87 ± 14
2LN	97.3 ± 3.6	7.7 ± 0.3	1.09 ± 0.12	88 ± 9[8]
5LN	98.1 ± 2.7	7.9 ± 0.3	1.08 ± 0.18	89 ± 19
10LN	89.0 ± 3.4	6.9 ± 0.4	0.78 ± 0.14	96 ± 9

NZSP: $Na_{3.4}Zr_2Si_{2.4}P_{0.6}O_{12}$; LN: $LaNbO_4$.

nm were taken as representative values of *E* and *H*.

For micropillar splitting, at least six micropillars were fabricated and tested for each composition. To avoid pore-related effects, micropillars were milled from pore-free regions [Figure 4D and E]. The parameters used for fracture toughness calculations are listed in Supplementary Table 3. For pristine NZSP, the pillar radius and critical splitting load were taken from[25], while the K_{IC} analysis was updated using the more accurately determined *E*/*H* ratio obtained in the present study. Compared with pristine NZSP, all LN-modified samples sustain markedly higher critical loads, and the calculated fracture toughness follows a consistent trend. Among all LN-modified samples, 2LN and 5LN achieve the highest fracture toughness values of 1.09 ± 0.12 and 1.08 ± 0.18 MPa·m$^{0.5}$, respectively.

The fracture strength was measured by ring-on-ring bending tests. A tendency toward higher fracture strength was observed for the LN-modified samples compared with pristine NZSP. No statistically significant differences were detected among the LN-modified samples (see Supplementary Table 4). For comparison, Nonemacher *et al.* reported decreasing *E* and *H* with increasing Al/Y substitution in NZSP, whereas the LN-modified NZSP in this work shows an *E* about 11% higher than the highest reported value of 88 GPa[18],

which is consistent with the enhanced stiffness associated with the observed intergranular and microstructural evolution in this work. They reported K_{IC} values of approximately 1.4-1.6 MPa·m$^{0.5}$ using Vickers indentation, about 28%E-47% higher than the maximum value of 1.09 ± 0.12 MPa·m$^{0.5}$ obtained here by micropillar splitting. Vickers indentation determines K_{IC} using an empirical equation based on the measured crack length and is therefore sensitive to irregular crack propagation and uncertainties in crack-length measurement. In contrast, micropillar splitting determines K_{IC} from the critical splitting load without requiring direct crack-length measurement. In addition, Go *et al.* measured a fracture strength of 73 ± 3 MPa for $Na_3Zr_2Si_2PO_{12}$ (H-NASICON) using a three-point bending test[27]. The mean fracture strength of 2LN in this study is approximately 20% higher than this reported value, which may partly reflect differences in microcrack density. However, the two materials differ in chemical composition, and the three-point bending test mainly produces uniaxial tensile stress, whereas the ROR test produces biaxial tensile stress. The two methods therefore differ in their sensitivity to flaw location and orientation, and the fracture-strength values should be compared with caution.

Defect-controlled mechanical enhancement

The improvements in mechanical properties observed in LN-modified NZSP can first be related to the evolution of microstructural features, particularly porosity, microcracks, and grain size. The reduction in porosity improves load-transfer continuity and reduces local stress concentrations, suppressing crack initiation and propagation. Pre-existing microcracks act as mechanically compliant defects that reduce the effective load-bearing capacity of the material[28,29].

As discussed above, the newly formed $Na_3LaP_2O_8$ phase and Nb-rich intergranular regions in the LN-modified samples effectively reduce the number of microcracks and residual pores and promote a more uniform grain-size distribution. These microstructural improvements are consistent with the increases observed in elastic modulus, hardness, fracture toughness, and mean fracture strength for the 2LN and 5LN samples. The 10LN sample exhibits higher porosity and a renewed increase in microcrack density, accompanied by reductions in its local mechanical properties (E, H, and K_{IC}). The observed differences in E, H, and K_{IC} are based on measurements from one representative pellet per composition, and their reproducibility across independently prepared pellets was not assessed.

Possible thermodynamic implications of Nb segregation at grain boundaries

In addition to defect reduction, Nb enrichment at grain boundaries and triple junctions may contribute to the mechanical enhancement through its influence on interfacial energetics. Previous TEM-EDX observations revealed pronounced Nb enrichment at triple junctions and along grain boundaries in the same material system[8]. According to the Gibbs adsorption theorem, solute segregation at interfaces can reduce the interfacial free energy[30], suggesting that Nb enrichment may lower the grain-boundary energy, although this effect has not been quantified in the present study.

In polycrystalline ceramics, the grain-boundary separation work W_{sep} can be expressed by[31]:

(5)

W_{sep} describes the energetic resistance to grain-boundary separation, where γ_{FS} is the free surface energy and γ_{GB} is the grain-boundary energy. If Nb segregation lowers γ_{GB} without a comparable reduction in γ_{FS}, W_{sep} could increase, potentially contributing to enhanced grain-boundary cohesion. This thermodynamic interpretation is proposed as a possible mechanism.

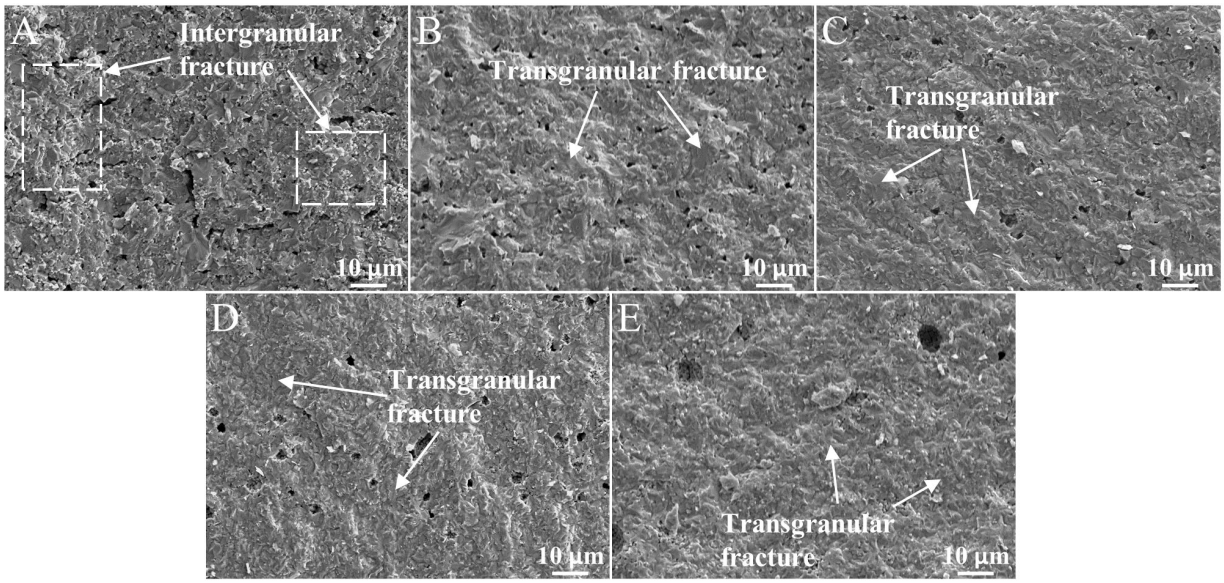


Figure 5. SEM images of fracture surfaces of (A) pristine NZSP; (B) 1LN; (C) 2LN; (D) 5LN; and (E) 10LN samples. The LN-modified NZSP samples exhibit predominantly transgranular fracture. SEM: Scanning electron microscope; NZSP: $Na_{3.4}Zr_2Si_{2.4}P_{0.6}O_{12}$; LN: $LaNbO_4$.

This hypothesis is consistent with the observed fracture behavior. Representative fracture surface morphologies are shown in Figure 5. In pristine NZSP, stacked and intact grains with well-defined grain boundaries are observed (Figure 5A, arrows), suggesting a predominantly intergranular fracture with only limited transgranular regions. In contrast, LN-modified NZSP samples exhibit extensively cleaved grains, indicating a transition toward predominantly transgranular fracture [Figure 5B-E]. This transition is consistent with strengthened grain-boundary cohesion and increased resistance to grain-boundary separation, which may contribute to the higher mean fracture strength observed for the LN-modified NZSP samples compared with pristine NZSP.

Ionic transport response to intergranular and microstructural evolution

Figure 6 shows the geometry-normalized impedance spectra of the pristine NZSP and the LN-modified samples. The LN-modified samples exhibit smaller semicircles than pristine NZSP, indicating a reduced grain-boundary resistive contribution. The spectra were fitted using an equivalent circuit, in which the high-frequency intercept R1 was assigned to the bulk contribution, while the R2-CPE2 element was attributed to the grain-boundary response. The geometry-normalized resistance values R_{bulk}, R_{gb}, and R_{total}, together with the corresponding ionic conductivities, are summarized in Table 4.

As shown in Table 4, R_{bulk} remains nearly constant for all samples except 10LN, whereas R_{gb} varies substantially with LN content. All LN-modified NZSP samples yield lower R_{gb} than pristine NZSP. This contrast suggests that the variation in total ionic conductivity among the examined samples is primarily associated with changes in grain-boundary transport rather than bulk conduction. Among them, 2LN shows the lowest R_{gb} and achieves a remarkably high total ionic conductivity (σ_{total}) of 9.3×10^{-3} S/cm. The particularly low grain-boundary resistance of 2LN likely reflects its lower porosity and microcrack density and improved grain-boundary continuity, which facilitate Na^+ transport across grain boundaries.

Notably, among the samples examined, ionic conductivity and mechanical properties exhibit different responses to increasing LN content. With further LN addition, the increased presence of insulating $Na_3LaP_2O_8$ progressively offsets the transport benefit of microstructural improvement, causing the conductivity to decrease beyond 2LN. At 10LN, the higher amount of insulating $Na_3LaP_2O_8$, together with

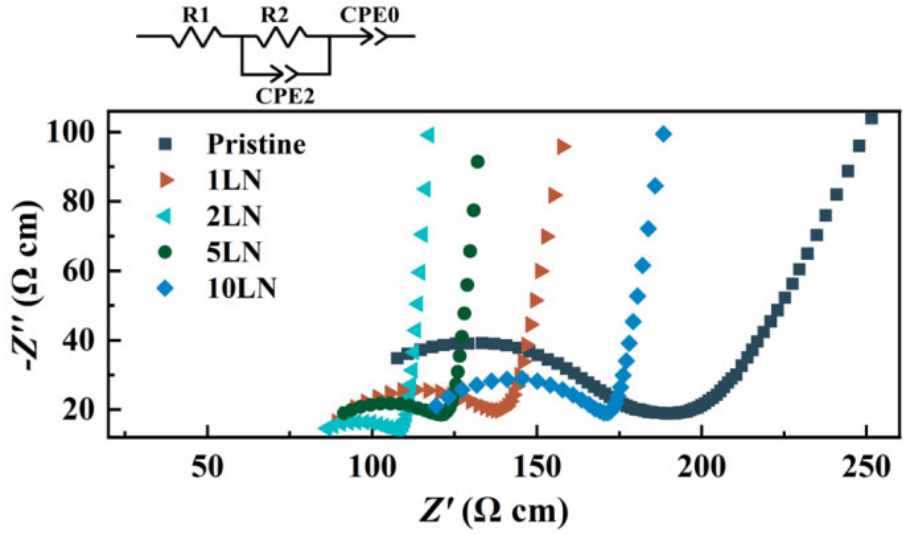


Figure 6. Nyquist plot of geometry-normalized impedance spectra recorded at RT together with the equivalent-circuit model used for fitting. Here, R and CPE denote resistance and constant phase element, respectively. The impedance data for pristine NZSP and 2LN were taken from Ref.[8]. LN: $LaNbO_4$; NZSP: $Na_{3.4}Zr_2Si_{2.4}P_{0.6}O_{12}$; CPE: constant phase element.

Table 4. Geometry-normalized bulk, grain-boundary, and total resistance values and the corresponding ionic conductivities

Sample	R_{bulk} (Ω cm)	R_{gb} (Ω cm)	R_{total} (Ω cm)	σ_{bulk} (S/cm)	σ_{total} (S/cm)
Pristine[8]	67	125	192	1.5×10^{-2}	5.2×10^{-3}
1LN	74	64	138	1.4×10^{-2}	7.2×10^{-3}
2LN[8]	69	39	108	1.4×10^{-2}	9.3×10^{-3}
5LN	72	49	121	1.4×10^{-2}	8.3×10^{-3}
10LN	101	71	172	9.9×10^{-3}	5.8×10^{-3}

LN: $LaNbO_4$.

increased porosity and microcracks, further hinders ionic transport. These results show that ionic transport and mechanical properties share a common microstructural basis but exhibit different sensitivities to intergranular and microstructural evolution: ionic transport becomes increasingly limited by insulating $Na_3LaP_2O_8$; the mechanical response is more closely associated with microstructural defects.

CONCLUSIONS

The effects of nominal $LaNbO_4$ modification on the microstructure and mechanical properties of NZSP solid electrolytes are systematically investigated. The results show that LN reacts with NZSP during processing, forming $Na_3LaP_2O_8$ and Nb-rich intergranular regions. $Na_3LaP_2O_8$ is distributed between grains and contributes to a more uniform grain structure and reduced microcrack density. The Nb-rich intergranular regions are associated with improved densification and may contribute to grain-boundary cohesion. Among the samples examined, the NZSP sample with 2 mol% nominal $LaNbO_4$ exhibits a 79% increase in ionic conductivity and substantially enhanced mechanical properties, including increases of 14% in elastic modulus, 40% in hardness, and 82% in fracture toughness, together with an 11% higher mean fracture strength compared with pristine NZSP. As the LN content increases beyond 2LN, ionic conductivity decreases, while the fracture toughness of 10LN falls below that of 2LN and 5LN. Specifically, the fracture toughness of 10LN is approximately 28% lower than that of 2LN but remains 30% higher than that of pristine NZSP. Overall, these findings highlight a microstructure-mechanics-transport relationship in the investigated pristine and LN-modified NZSP samples.

DECLARATIONS

Acknowledgements

The authors thank Dr. D. Grüner and Mr. M. Ziegner for their support with SEM, EDX, and XRD analyses, and Ms. T. Osipova for assistance with bending tests.

Authors' contributions

Writing - original draft: Liu, X.
Data curation: Liu, X.; Ma, Q.
Investigation: Liu, X.; Ma, Q.
Formal analysis: Liu, X.
Visualization: Liu, X.
Conceptualization: Ma, Q.; Malzbender, J.
Methodology: Malzbender, J.
Project administration: Malzbender, J.
Supervision: Malzbender, J.; Schwaiger R.
Resources: Schwaiger R.
Writing - review and editing: Tietz, F.; Malzbender, J.; Schwaiger R.

Availability of data and materials

Some results supporting this study are presented in the Supplementary Materials. Other raw data that support the findings of this study are available from the corresponding author upon reasonable request.

AI and AI-assisted tools statement

During the preparation of this manuscript, the AI tool ChatGPT Plus (OpenAI; GPT-5.6 Sol, released 2026-07-09) was used to generate selected schematic elements of the graphical abstract using OpenAI's gpt-image model. The tool did not influence the study design, data collection, analysis, interpretation, or the scientific content of the work. All authors take full responsibility for the accuracy, integrity, and final content of the manuscript.

Financial support and sponsorship

Liu, X. acknowledges financial support from the China Scholarship Council (No. 202308120016).

Conflicts of interest

Ma, Q. is an Associate Editor of the journal *Energy Z* but was not involved in any steps of editorial processing, notably including reviewer selection, manuscript handling, and decision-making. Liu, X.; Ma, Q.; Tietz, F.; Malzbender, J.; Schwaiger R. are affiliated with Forschungszentrum Jülich GmbH.

Ethical approval and consent to participate

Not applicable.

Consent for publication

Not applicable.

Copyright

© The Author(s) 2026.

Supplementary Materials

Supplementary Materials

REFERENCES

1. Wang, Y.; Ou, R.; Yang, J.; et al. The safety aspect of sodium ion batteries for practical applications. *J. Energy. Chem.* **2024**, *95*, 407-27. DOI
2. Liang, S.; Heng, Y.; Wang, C. Thermal stability and safety challenges of all-solid-state batteries. *Energy. Z.* **2026**, *2*, 200006. DOI

3. Sarfraz, N.; Kanwal, N.; Ali, M.; et al. Materials advancements in solid-state inorganic electrolytes for highly anticipated all solid Li-ion batteries. *Energy. Storage. Mater.* **2024**, *71*, 103619. DOI
4. Roh, J.; Do, N.; Lee, H.; et al. Towards practical all-solid-state batteries: structural engineering innovations for sulfide-based solid electrolytes. *Energy. Mater.* **2025**, *5*, 500061. DOI
5. Nayak, P. K.; Yang, L.; Brehm, W.; Adelhelm, P. From lithium-ion to sodium-ion batteries: advantages, challenges, and surprises. *Angew. Chem. Int. Ed. Engl.* **2018**, *57*, 102-20. DOI PubMed
6. Lu, Y.; Li, L.; Zhang, Q.; Niu, Z.; Chen, J. Electrolyte and interface engineering for solid-state sodium batteries. *Joule* **2018**, *2*, 1747-70. DOI
7. Li, S.; Zhao, Y.; Dang, Q.; Qin, J.; Hu, Q. Research progress on LT performance of sodium-ion battery electrolytes. *Energy. Mater.* **2026**, *6*, 600021. DOI
8. Liu, L.; Liu, Y.; Zhou, X.; et al. Nominal lanthanum niobate, a versatile additive for reducing grain boundary resistance in conductive ceramics. *Adv. Energy. Mater.* **2025**, *15*, 2404985. DOI
9. Ponrouch, A.; Marchante, E.; Courty, M.; Tarascon, J.; Palacín, M. R. In search of an optimized electrolyte for Na-ion batteries. *Energy. Environ. Sci.* **2012**, *5*, 8572. DOI
10. Tseng, K.; Fang, Z.; Wang, B.; et al. Reactive hot-pressed $Na_{3.4}Zr_2Si_{2.4}P_{0.6}O_{12}$: nanoscale grains, glass-free microstructure, high total conductivity, enhanced chemical stability. *J. Mater. Chem. A.* **2025**, *13*, 34706-20. DOI
11. Darjazi, H.; Falco, M.; Colò, F.; et al. Electrolytes for sodium ion batteries: the current transition from liquid to solid and hybrid systems. *Adv. Mater.* **2024**, *36*, e2313572. DOI
12. Zhang, Q.; Zhou, Q.; Lu, Y.; et al. Modification of NASICON electrolyte and its application in real Na-ion cells. *Engineering* **2022**, *8*, 170-80. DOI
13. Oh, J. A. S.; He, L.; Plewa, A.; et al. Composite NASICON ($Na_3Zr_2Si_2PO_{12}$) solid-state electrolyte with enhanced Na^+ ionic conductivity: effect of liquid phase sintering. *ACS. Appl. Mater. Interfaces.* **2019**, *11*, 40125-33. DOI
14. Ke, X.; Wang, Y.; Ren, G.; Yuan, C. Towards rational mechanical design of inorganic solid electrolytes for all-solid-state lithium ion batteries. *Energy. Storage. Mater.* **2020**, *26*, 313-24. DOI
15. Campbell, C. J.; Monismith, S.; Raj, V.; et al. Reactive carbide-based synthesis and microstructure of NASICON sodium metal all solid-state electrolyte. *Adv. Mater.* **2026**, *38*, e12961. DOI
16. Wolfenstine, J.; Go, W.; Kim, Y.; Sakamoto, J. Mechanical properties of NaSICON: a brief review. *Ionics* **2023**, *29*, 1-8. DOI
17. Lin, T.; Wu, H. B. Rethinking dendrite growth in solid electrolytes. *Energy. Z.* **2026**, *2*, 200009. DOI
18. Nonemacher, J. F.; Naqash, S.; Tietz, F.; Malzbender, J. Micromechanical assessment of Al/Y-substituted NASICON solid electrolytes. *Ceram. Int.* **2019**, *45*, 21308-14. DOI
19. Hitesh, B.; Sil, A. Effect of sintering and annealing on electrochemical and mechanical characteristics of $Na_3Zr_2Si_2PO_{12}$ solid electrolyte. *J. Am. Ceram. Soc.* **2023**, *106*, 6743-54. DOI
20. Schneider, C. A.; Rasband, W. S.; Eliceiri, K. W. NIH Image to ImageJ: 25 years of image analysis. *Nat. Methods.* **2012**, *9*, 671-5. DOI PubMed PMC
21. Irvine, J. T. S.; Sinclair, D. C.; West, A. R. Electroceramics: characterization by impedance spectroscopy. *Adv. Mater.* **1990**, *2*, 132-8. DOI
22. Sebastiani, M.; Johanns, K.; Herbert, E.; Carassiti, F.; Pharr, G. A novel pillar indentation splitting test for measuring fracture toughness of thin ceramic coatings. *Philos. Mag.* **2015**, *95*, 1928-44. DOI
23. Sebastiani, M.; Johanns, K.; Herbert, E.; Pharr, G. Measurement of fracture toughness by nanoindentation methods: recent advances and future challenges. *Curr. Opin. Solid. St. M.* **2015**, *19*, 324-33. DOI
24. ASTM International. C1499-05: Standard test method for monotonic equibiaxial flexural strength of advanced ceramics at ambient temperature. 2005, West Conshohocken. DOI
25. Liu, X.; Gross, J. P.; Ma, Q.; Tietz, F.; Malzbender, J.; Schwaiger, R. $Na_3LaP_2O_8$-enabled microstructural engineering for enhanced mechanical robustness and ionic transport behavior in NaSICON solid electrolytes. *J. Mater. Chem. A.* **2026**, *14*, 18101-11. DOI
26. Jackman, S. D.; Cutler, R. A. Effect of microcracking on ionic conductivity in LATP. *J. Power. Sources.* **2012**, *218*, 65-72. DOI
27. Go, W.; Kim, J.; Pyo, J.; Wolfenstine, J. B.; Kim, Y. Investigation on the structure and properties of $Na_{3.1}Zr_{1.55}Si_{2.3}P_{0.7}O_{11}$ as a solid electrolyte and its application in a seawater battery. *ACS. Appl. Mater. Interfaces.* **2021**, *13*, 52727-35. DOI
28. Fan, X.; Case, E. D.; Baumann, M. J. The effect of indentation-induced microcracks on the elastic modulus of hydroxyapatite. *J. Mater. Sci.* **2012**, *47*, 6333-45. DOI
29. Buljak, V.; Serrano-Munoz, I.; Kupsch, A.; et al. On the closure of thermally induced micro-cracks in aluminum titanate ceramics. *Ceram. Int.* **2025**, *51*, 55141-52. DOI
30. Wynblatt, P.; Rohrer, G.; Papillon, F. Grain boundary segregation in oxide ceramics. *J. Eur. Ceram. Soc.* **2003**, *23*, 2841-8. DOI

31. Rice, J. R.; Wang, J. Embrittlement of interfaces by solute segregation. *Mat. Sci. Eng. A-Struct.* **1989**, *107*, 23-40. DOI

Disclaimer/Publisher's Note: All statements, opinions, and data contained in this publication are solely those of the individual author(s) and contributor(s) and do not necessarily reflect those of OAE and/or the editor(s). OAE and/or the editor(s) disclaim any responsibility for harm to persons or property resulting from the use of any ideas, methods, instructions, or products mentioned in the content.



© The Author(s) 2026. Open Access This article is licensed under a Creative Commons Attribution 4.0 International License (https://creativecommons.org/licenses/by/4.0/), which permits unrestricted use, sharing, adaptation, distribution and reproduction in any medium or format, for any purpose, even commercially, as long as you give appropriate credit to the original author(s) and the source, provide a link to the Creative Commons license, and indicate if changes were made.